PAPER

Covert-inspired flaps for lift enhancement and stall mitigation

To cite this article: Chengfang Duan and Aimy Wissa 2021 *Bioinspir. Biomim.* **16** 046020

View the article online for updates and enhancements.

Bioinspiration & Biomimetics

PAPER

Covert-inspired flaps for lift enhancement and stall mitigation

Chengfang Duan and Aimy Wissa*

University of Illinois at Urbana-Champaign, 105 S. Mathews Ave., Urbana, IL 61801, United States of America
* Author to whom any correspondence should be addressed.

**E-mail:** awissa@illinois.edu

Abstract

Even though unmanned aerial vehicles (UAVs) are taking on more expansive roles in military and commercial applications, their adaptability and agility are still inferior to that of their biological counterparts like birds, especially at low and moderate Reynolds numbers. A system of aeroelastic devices used by birds, known as the covert feathers, has been considered as a natural flow-control device for mitigating flow separation, enhancing lift, and delaying stall. This study presents the effects of a covert-inspired flap on two airfoils with different stall characteristics at Reynolds numbers in the order of 10^5, where small scale UAVs operate. Detailed experiments and simulations are used to investigate how the covert-inspired flap affects lift and drag on an airfoil that exhibits sharp or sudden stall (i.e. the NACA 2414 airfoil) and one that exhibits soft or gradual stall (i.e. an E387(A) airfoil). The effects of the flap chord-wise locations and deflection angles on lift and drag is investigated, through wind tunnel experiments, for two types of flaps namely, a freely-moving flap and a static flap. Results show that the static covert-inspired flap can delay stall by up to 5° and improve post-stall lift by up to 23%. However, the post-stall lift improvement characteristics and sensitivities are highly affected by the airfoil choice. For the soft stall airfoil (i.e. E387(A)), the stall onset delay is insensitive to changing the flap deflection angle, and the flap becomes ineffective when the flap location is changed. In contrast, for the sharp stall airfoil (i.e. NACA 2414), the post-stall lift improvements can be tuned using the flap deflection angle, and the flap remains effective over a wide range of chord-wise locations. Numerical studies reveal that the lift improvements are attributed to a step in the pressure distribution over the airfoil, which allows for lower pressures on the suction side upstream of the flap. The distinctions between the flap-induced lift enhancements on the soft and sharp stall airfoils suggest that the flap can be used as a tunable flow control device for the sharp stall airfoil, while for the soft stall airfoil, it can solely be used as a stall mitigation device that is either on or off.

Nomenclature

α	Angle of attack (AoA)
α_{stall}	Stall angle of attack
C_l	Lift coefficient
$C_{l\text{max}}$	Maximum lift coefficient
C_d	Drag coefficient
C_p	Pressure coefficient
Re	Reynolds number
c	Chord
β	Flap deflection angle
l_{flap}	Flap length
x_{flap}	Flap root location

1. Introduction

The ability for small unmanned aerial vehicles (UAV) to perform complex maneuvers and to maintain control is becoming increasingly important as UAVs are taking on more expansive roles in military and commercial applications. Yet, despite advances in technology, UAVs' flight performance, such as agility and maneuverability, is still inferior to that of their biological counterparts like birds or insects [1, 2]. Both birds and small UAVs operate at similar Reynolds numbers (Re $\approx 10^4$–10^5) [2], where they are both susceptible to flow separation and stall. However, during the
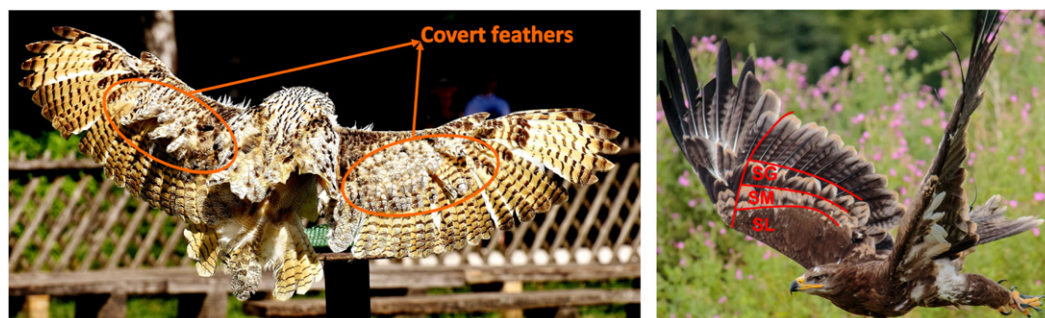
Figure 1. Coverts on the upper surface of an owl wing (left), reproduced from [7]. CC BY 4.0. and a steppe eagle wing (right), reproduced from [8]. CC BY 4.0.

Table 1. Summary of previous studies[a].

Paper reference	Study type	Reynolds number	Airfoil	ΔC_l/deg at α_{stall}	Flap design	Flap effects
Fang *et al* [17]	Numerical	1×10^3	NACA0012	N/A	Movable and static flap	Increase lift and reduce lift fluctuation
Wang *et al* [9]	Experimental	3.8×10^4	NACA0012	−0.24	Real feathers	Increase lift and lift-drag ratio
Brücker and Weidner [10]	Experimental	7.7×10^4	NACA0020	N/A	Flexible hairy flaps	Delay stall in airfoil ramp-up motion
Schlüter [18]	Experimental	$3–4 \times 10^5$	NACA0012 SD8020 NACA4412	−0.02 N/A −0.03	Movable flap	Increase the lift near stall
Johnston and Gopalarathnam [16]	Experimental	4×10^5	Customized airfoil	−0.04	Movable and static flap	Delay stall AoA
Bramesfeld and Maughmer [14]	Experimental	1×10^6	S824	−0.01	Movable flap	Increase maximum lift
Meyer *et al* [15]	Experimental/ numerical	1×10^6	HQ17	N/A	Movable and static flap	Increase maximum lift
Gardner *et al* [11]	Experimental/ numerical	1.1×10^6	OA209	N/A	Actuated movable flap	Reduce moment peak in dynamic stall
Bechert *et al* [12, 13]	Experimental	$1–2 \times 10^6$	HQ41	−0.02	Movable flap	Increase maximum lift
This study	Experimental/numerical	$1–2 \times 10^5$	E387(A) NACA2414	−0.08 −0.30	Movable and static flap	Increase post-stall lift

[a]N/A represents either the baseline airfoil $C_l−\alpha$ curve is not provided or is not showing significant lift drop.

same high AoA maneuvers that render UAVs inefficient (e.g. short-distance takeoffs and landings and flying through sudden gusts), birds use their feathers as deployable flow control devices. One of such feather systems is referred to as the coverts. Covert feathers make up a large portion of the total wing surface and provide all of the upper surface contours, and most of the lower surface contour over the thick forward sections of the wing [3]. There are several types of covert feathers (figure 1 (right)). The function of the covert feathers has been debated in both the engineering and biology communities.

In biology, some research efforts suggest that they operate similar to leading-edge Kruger flaps, while others claim that they act as vortex generators [4]. Recent studies based on free flight videos of a steppe eagle describe the covert feathers as nature's equivalent of wing aeroelastic devices [5]. For example,

during high AoA maneuvers, such as landing, takeoffs, and perching, the lesser covert (SL) feathers on the lower side of the wing deploy. While during gust conditions, the upper wing greater covert (SG) feathers deploy. Moreover, a study by Brown and Feede [6] measured the discharge of the mechanoreceptors at the base of the coverts. Their study suggests that coverts receptors may supply information related to the wing stall, supporting in-flight observations and reinforcing the role of the coverts in controlling flow separation and mitigating stall.

In engineering, due to their simple deployment mechanics and multi-functionality, the covert feathers have inspired the design of various flow control devices that can be used for lift improvement and stall mitigation. Covert-inspired devices presented in

the literature range from flaps made of real feathers and artificial hair-like fibers to rigid flaps of various geometries [9–11]. Flaps with various mobility have also been studied, where some flaps were allowed to rotate freely (i.e. freely-moving flaps), while others were rigidly attached to the surface of an airfoil (i.e. static flaps). Experimental and numerical studies on covert-inspired flap show lift enhancement especially at high AoA. Earlier studies by Bechert *et al* [12, 13] investigated the effects of a freely-moving flap on a laminar glider wing, and observed lift improvement up to 18%. Freely-moving flaps on an airfoil suction surface were also studied by Bramesfeld and Maughmer [14] at Re $= 1 \times 10^6$. Results show that the flaps increase the maximum lift. The lift enhancement was attributed to a 'pressure dam' effect, which allows for lower pressures upstream of the flap. More recently, Meyer *et al* [15] studied an HQ17 airfoil with a single freely-moving flap and a static flap using both wind tunnel experiments and hybrid Reynolds-averaged Navier–Stokes equations (RANS)/large eddy simulation (LES) simulations at Re $= 1 \times 10^6$. The authors show that for certain flap configuration, C_{lmax} is enhanced by more than 10%, and the stall is delayed. The authors attributed these results to the flap's ability to prevent reversed flow from advancing towards the leading edge of the airfoil. At the Reynolds numbers of interest to this study (i.e. Re $\approx 10^5$), Johnston and Gopalarathnam [16] studied the effects of a freely-moving and a static flap on a custom-designed airfoil at Re $= 4 \times 10^5$. Their results show that the stall was delayed by $4°$–$8°$, but no change was observed in C_{lmax}. There are also a few studies that have investigated the effect of covert-inspired flaps at lower Reynolds numbers ($10^3 \leqslant$ Re $\leqslant 10^4$) showing similar lift improvements [9, 17, 18].

Table 1 summarizes previous engineering studies on covert-inspired flaps, including the study type, Reynolds number, airfoil section, and the flap design and over all aerodynamic effect. The table also shows the C_l drop rate at α_{stall} of the baseline airfoils studied in the literature. These values were obtained by taking the numerical derivative of the C_l–α data at α_{stall}, so that the stall sharpness can be quantified. From the table, it is clear that although many studies have shown the effect of covert-inspired flaps on lift, most of them focused on baseline airfoils with soft stall characteristics. Soft stall refers to a gradual loss of lift beyond the maximum lift AoA. This stall behavior results from the separation location moving gradually towards the leading edge as the wing AoA increases. In this paper, we extend the understanding of the effect of covert-inspired flaps on lift and drag by examining two baseline airfoils with different stall characteristics namely, soft stall airfoil (E387(A), ΔC_l/deg at $\alpha_{stall} = -0.08$) and a sharp stall airfoil (NACA 2414, ΔC_l/deg at $\alpha_{stall} = -0.30$).

Numerical simulations and wind tunnel experiments are performed at the Reynolds number of 2×10^5 because it is relevant to both avian flight and small scale UAVs. The remainder of the paper is arranged as follows: section 2 reports the experimental and the numerical methods. Section 3 presents experimental and numerical results of both the soft stall airfoil and the sharp stall airfoil. Lastly, section 4 summarizes and discusses the key finding of this work.

2. Methods

2.1. Experimental methods

2.1.1. Wind tunnel setup
The experiments were conducted in the Talbot Laboratory wind tunnel of the University of Illinois at Urbana-Champaign, which is a closed-section, open-loop, constant pressure wind tunnel as described in [19]. The wind tunnel has a cross-section of 90 cm wide and 45 cm high. The wing assembly (figure 2(a)) was mounted horizontally in the wind tunnel section with one side mounted to the test section wall, and the other side attached to a splitter plate, as shown in figure 2(b). The splitter plate was used to achieve a preferable 2D test section, of which the height is longer than its width to minimize the effects that the upper and lower test section walls have on the curvature of the streamlines [20]. The freestream flow velocity was measured by a standard pitot-static tube, which was placed upstream of the wing, between the splitter plate and the wind tunnel wall. Velocity correction was applied following the method provided by Giguère and Selig [20].

The integrated aerodynamic forces (i.e. lift and drag) were measured using an ATI gamma six-axis force/torque transducer, which has a range of 0–32 N, a resolution of 1/160 N. The force/torque transducer has maximum uncertainties of 0.75% in the X and Y axes, when measuring at the full scale. A Velmex B48 rotary table with a stepper motor was used to change the wing AoA with a precision of 0.0125°. Since the force/torque transducer was rotated with the wing assembly, a rotation matrix with mass compensation was applied to the force data in the X and Y axes so that the net lift and drag forces at each AoA can be obtained [21]. During each test, the force data was collected at a sampling frequency of $f = 250$ Hz for 10 seconds at each AoA, and the data was averaged to determine the lift and drag data. Wind tunnel wall corrections, including solid blockage, wake blockage, and streamline curvature, were applied to the lift and drag coefficients [22].

2.1.2. Test configurations and matrix
Two airfoils were tested in the wind tunnel, namely an E387(A) and an NACA 2414. These airfoils were selected because while both airfoils are designed for moderate Reynolds number flight [23], they exhibit
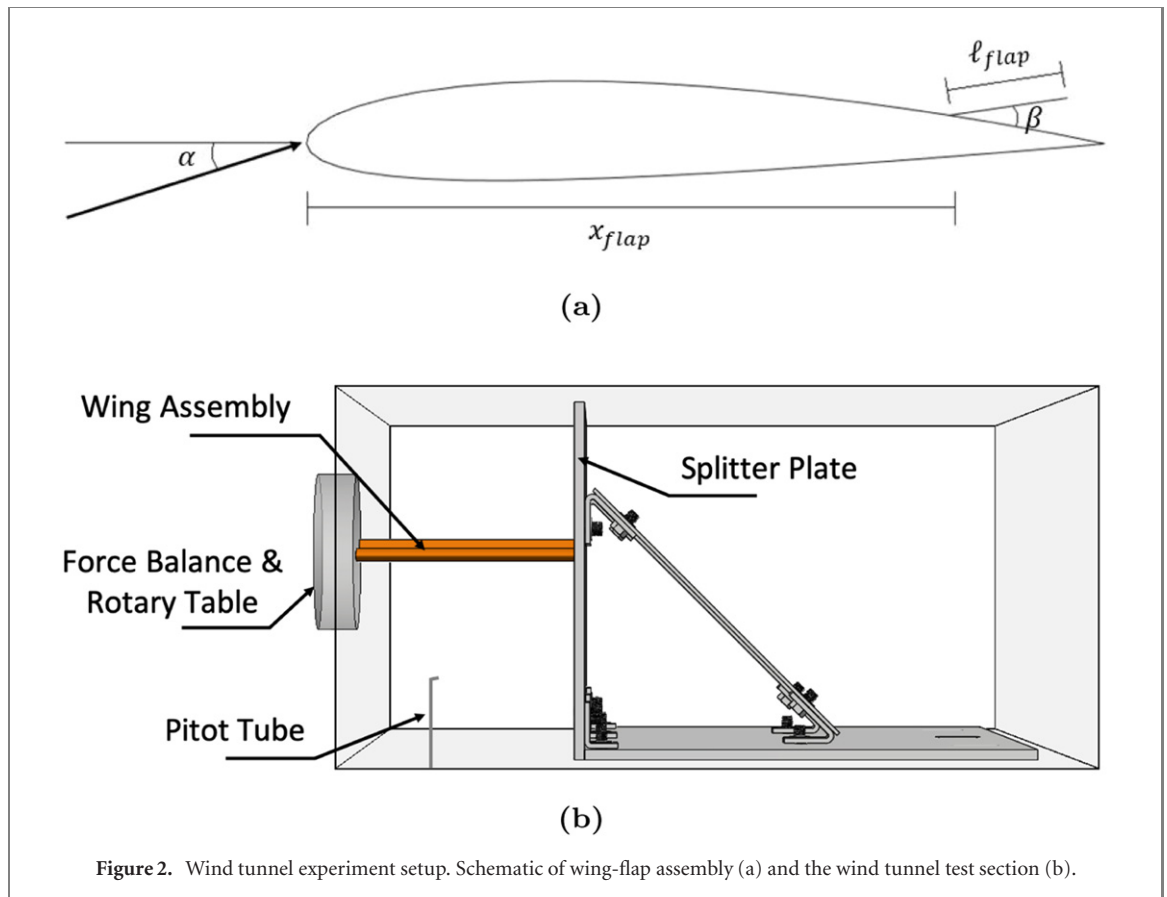
Figure 2. Wind tunnel experiment setup. Schematic of wing-flap assembly (a) and the wind tunnel test section (b).

different stall behaviors (figure 3). The E387(A) has a soft stall, where the lift drop and drag increase is gradual beyond the stall AoA. The E387(A) is similar to the other airfoils studied in the literature [14–16]. On the other hand, the NACA 2414 has a sharp stall airfoil, defined as an abrupt loss in the lift and increase in drag after the maximum lift AoA. Airfoils with such stall behavior have not been considered before as the baseline for the covert-inspired flaps. The lift curves in figure 3 show a comparison between the lift reported in [23] (dashed lines) and measured during this study (solid lines). The figure shows good overall agreement, thus validating the measurement in this study. The offset between the results in reference [23] and our experimental results are slightly larger for the E387(A) compared to the NACA 2414 airfoil. This discrepancy could be due to wing manufacturing variations since the E387(A) airfoil trailing edge is much thinner than the NACA 2414 airfoil. The airfoil sections tested in this study still exhibit the desired distinctive stall characteristics, including the stall AoA and stall behavior, thus could serve as appropriate baselines to understand the effect of the coverts on two baselines with different stall behaviors.

The wing test section has a chord length of 120 mm and a span of 280 mm and was fabricated using a stereolithography (SLA) 3D printer. The flap was water-jet cut from a 6061 aluminum sheet with a thickness of 1 mm to ensure rigidity. The root of the flap was hinged on the suction surface of the wing

using 1 mil-thick Kapton tape. Two types of flap were studied: a static flap and a freely-moving flap. For the static flap configurations, the flap deflection angles, β, were fixed using small wedges. The flap deflection angle is defined as the angle between the flap and the tangent line of the upper surface of the airfoil from the root of the flap. For the freely-moving flap configuration, the flap was allowed to rotate freely about the hinge.

The flap length and locations were selected based on several designs in the literature [9–11, 14–16]. The flap length, ℓ_{flap}, was held constant at 15% of chord length. However, the limits of the flap deflection angles and locations were determined through preliminary tests. The static flaps were tested at several deflection angles. The maximum flap deflection angles for the static flaps were 60° and 45° for NACA 2414 and E387(A), respectively. Both the static and freely-moving flaps were tested at various chord-wise locations. More specifically, four flap locations, x_{flap}, defined as the distance from the root of the flap to the leading edge of the airfoil along the chord line, were tested during these experiments, namely 0.4c, 0.6c, 0.7c, and 0.8c. There are two additional flap locations tested for the sharp stall airfoil (NACA 2414) because when the location of the flap approached the airfoil leading edge of the soft stall airfoil, the flap became ineffective at improving lift. More specifically, the flap started to become ineffective at 0.7c for the E387(A) airfoil, while the flaps on the sharp stall airfoil stayed
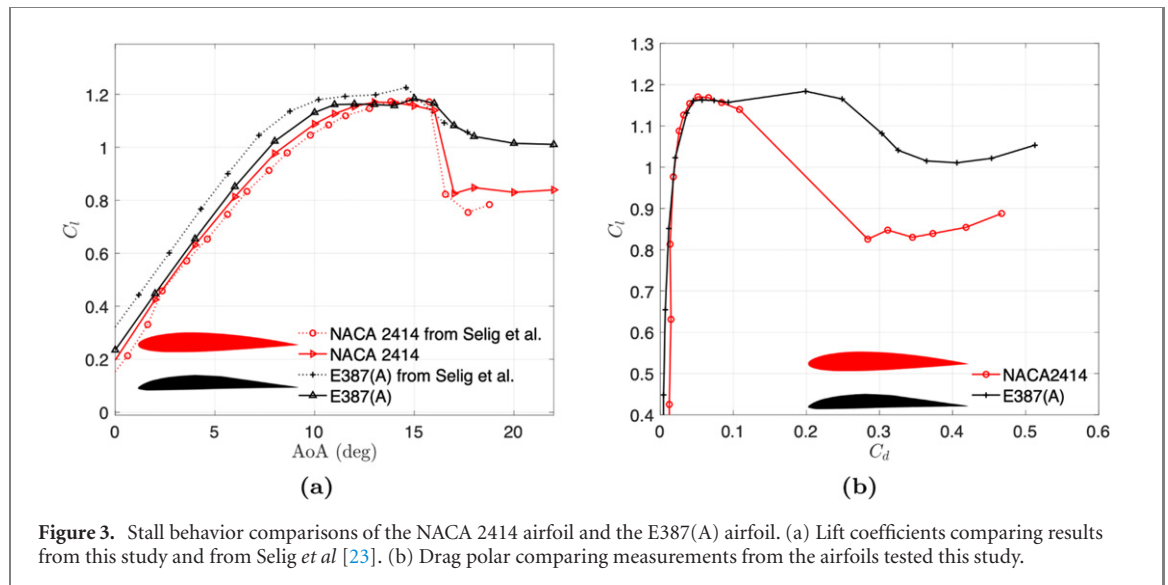
Figure 3. Stall behavior comparisons of the NACA 2414 airfoil and the E387(A) airfoil. (a) Lift coefficients comparing results from this study and from Selig *et al* [23]. (b) Drag polar comparing measurements from the airfoils tested this study.

effective until $0.4c$. The experimental matrix is shown in table 2. All configurations were tested at a Reynolds number of 1×10^5 and 2×10^5. The results from both Reynolds numbers were very similar, therefore the next section presents results for $\text{Re} = 2 \times 10^5$ only.

A naming convention was also established to distinguish the various flap configurations. Four-digit names were used to identify the static flap configurations. The first two digits indicate the normalized flap location, and the last two digits indicate the static flap deflection angle. For example, a static flap located at $0.8c$ and deflected at $15°$ is named '8015'. The freely-moving flaps configuration were named using 2 digits to indicate the flap location and the word 'free' to indicate that the flap's rotation was unconstrained. For example, a freely-moving flap located at $0.7c$ is referred to as '70free'.

2.2. Numerical methods

Complementary numerical simulations were carried out for both airfoils with a static flap located at $0.8c$ and Reynolds number of 2×10^5. A 3D detached eddy simulation (DES), which is a hybrid RANS–LES method, was used in this study to capture the massively separated flow over the airfoil. An unsteady RANS model is deployed in the near-wall flow region, while a LES treatment is applied to the separated flow regions. Thus, the DES approach can model the separated flow region with relatively low computational cost [24]. In this study, a 3D DES with the Spalart–Allmaras turbulence model was conducted using ANSYS Fluent 2019R2 on a workstation with an Intel i9-9920X processor and 64 GB memory.

The side view of the computational domain along with the boundary conditions is shown in figure 4(a). The airfoil leading edge was placed on the center of the semi-circle which has a radius of 10 chords. A velocity inlet with a turbulent viscosity ratio of 10 was imposed on the top and bottom boundaries of the computational domain on the top and bottom.

The flow outlet on the right had a pressure outlet boundary condition with a gauge pressure of 0 Pa. The pressure outlet is 10 chords away from the airfoil leading edge. The no-slip wall boundary condition was applied to the airfoil and the flap. The span-wise length was equal to the chord of the airfoil as suggested in [24], and the span-wise boundaries were periodic. The hybrid structured/unstructured mesh used in the simulations is shown in figures 4(b) and (c). Around the airfoil, 12 inflation layers composed the structured grid, and 200 nodes were arranged along the airfoil surface. The near-wall grid spacing was less than 7.5×10^{-4} chord for a wall function close to 1. In the span-wise direction, the sweep mesh method was applied with a division number of 30 to ensure that the span-wise mesh is homogeneous. The mesh contains over 1 million nodes in total. The time step was 7.5×10^{-3} s, which is around $0.025 * c/U_\infty$ as suggested in [24]. The second-order upwind method was used for the spatial discretization and the bounded seconded-order implicit scheme was used for the temporal discretization. The convergence criteria for the residuals were set to be 10^{-5}. The simulations were terminated after around 100 chords of travel to ensure that no significant change in the lift-force time history is observed. The numerical results along with the validation against the experimental results are shown in the next section.

To further examine the difference between the stall behavior of both airfoils, the numerical simulations were used to predict the separation point for both baseline airfoils as a function of the AoA (figure 5). The separation location was predicted by finding the location on the airfoil suction side where the wall friction coefficients approach zero. Figure 5 shows that as the AoA increases, the two airfoils' separation location moves towards the leading edge at different rates. More specifically, when the AoA increases from $13°$ to $20°$, the separation location on the suction surface of the NACA 2414 airfoil propagated upstream by $0.5c$,

Table 2. Wind tunnel test matrix showing the test parameters for both airfoils.

Airfoil	Reynolds number	Flap location	Flap deflection angle (or freely-moving)
E387(A)	2×10^5	0.7c, 0.8c	Freely-moving, 15°,30°,45°
NACA 2414	2×10^5	0.4c, 0.6c,0.7c, 0.8c	Freely-moving, 15°,30°,45°,60°
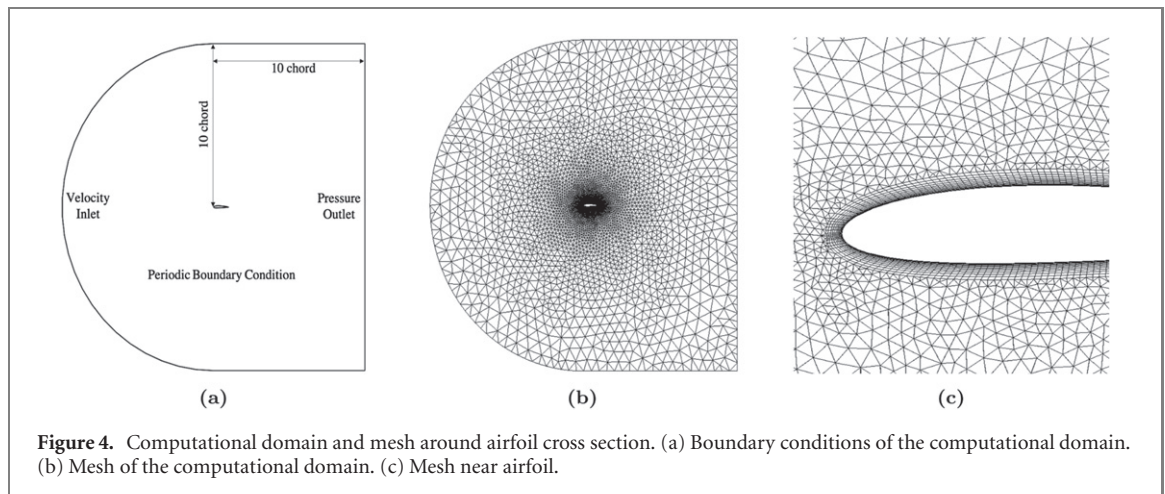
Figure 4. Computational domain and mesh around airfoil cross section. (a) Boundary conditions of the computational domain. (b) Mesh of the computational domain. (c) Mesh near airfoil.
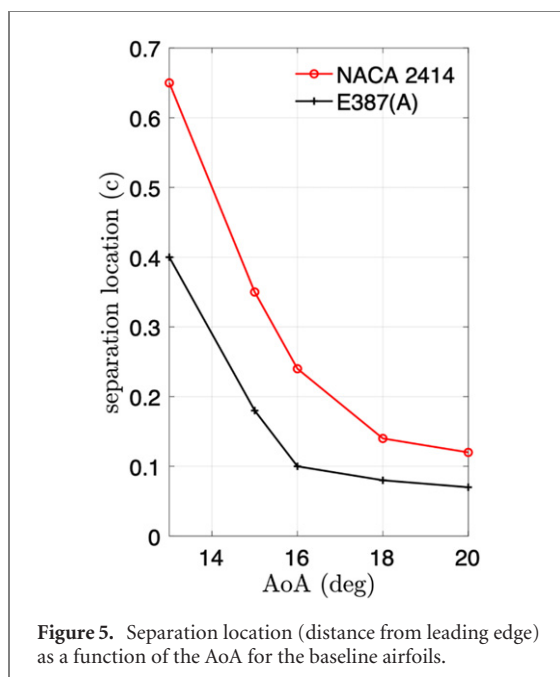
Figure 5. Separation location (distance from leading edge) as a function of the AoA for the baseline airfoils.

while the separation location of the E387(A) moves up by 0.3c only. Thus, for the same AoA increase, the separation location of the NACA2414 move towards the leading edge of the airfoil 40% more than the E387(A) airfoil. These results support the characterization of the E387(A) airfoil as a soft stall airfoil and the NACA2414 as a sharp stall airfoil. The next section presents the experimental and numerical results of the E387(A) airfoil followed by a discussion of the NACA2414 airfoil results.

3. Results and discussion

3.1. Soft stall airfoil results

The C_l–α and the C_l–C_d curves for the E387(A) airfoil with a flap located at 0.8c at Re $= 2 \times 10^5$ are shown in figure 6. The effect of the flap on lift and drag is different at pre-stall and post-stall AoA.

Flap effect at pre-stall conditions: at pre-stall angles of attack (AoA $< 15°$), the flap decreases lift and increases drag. Moreover, for the static flap configurations, increasing the flap deflection angles results in more loss in lift compared to the baseline airfoil. The freely-moving flap has a similar overall effect on the lift as the static flaps. However, the pre-stall lift penalty is less than any of the static flaps. These lift and drag results can be explained because at pre-stall AoA the flow is mostly attached or mildly separated. Even a small flap deflection is considered excessive and causes the flap to protrude into the high-velocity freestream. Thus, at pre-stall AoA, the flap acts similar to a spoiler and reduces these overall lift production [15]. The reduced lift penalties in the case of freely-moving flap can be attributed to the fact that the flap's rotation is activated by the suction pressure around the top surface of the airfoil. At low AoA and near the trailing edge of the airfoil, the suction pressure is minimal. Thus, the freely-moving flap remains mostly closed, reducing the lift penalty at the pre-stall regime. Some lift loss is still observed due to the slight flap deflection and the thickness of the flap, which introduces a discontinuity on the suction side of the airfoil even when the flap remains closed.
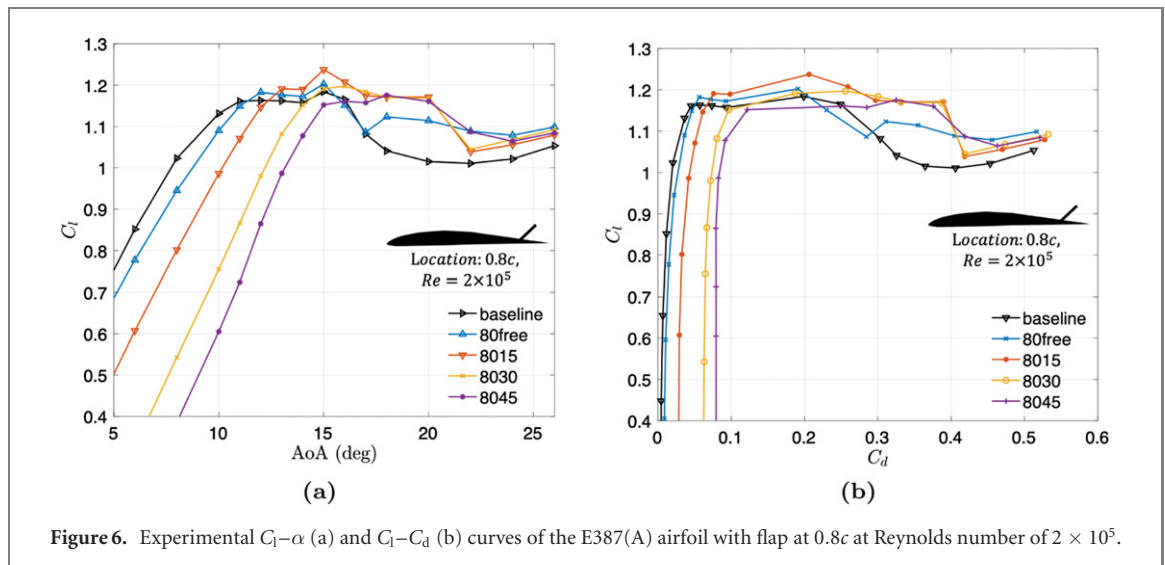
Figure 6. Experimental $C_l-\alpha$ (a) and C_l-C_d (b) curves of the E387(A) airfoil with flap at $0.8c$ at Reynolds number of 2×10^5.

Flap effect at post-stall conditions: at post-stall angles of attack (AoA > 15°), the flap mitigates the lift drop and maintains the maximum lift coefficient, C_{lmax}, for up to 5° beyond the baseline stall AoA (figure 6). The C_l-C_d curves (figure 6(b)) indicate that an airfoil with flap is more aerodynamically efficient at the post-stall condition. In the other words, the airfoil with the flap can produce similar lift as the baseline airfoil at a lower drag penalty. For the static flap configuration, at post-stall AoA, the lift is less sensitive to the flap deflection angle when compared to pre-stall AoA, such that different flap deflection angles resulted in similar lift improvement and stall delay. The freely-moving flap has a similar overall effect on the lift as the static flaps. However, the post-stall lift improvement is less than any of the static flaps.

The post-stall lift improvements can be explained by examining the pressure distribution around the airfoil. Figure 7 shows the numerical results of the time-averaged pressure distribution around the E387(A) baseline airfoil and the E387(A) airfoil with 8015 flap at AoA = 20°. For these two configurations, the integrated lift coefficients predicted by the simulations have relative errors of less than 3% when compared to the corresponding experimental results. The integrated area of C_p on the flap is much smaller than the integrated area of C_p on the airfoil. Thus, the flap's direct contribution to lift is negligible compared to how the flap affects the overall pressure distribution around the airfoil. More specifically, the flap introduces a step in the pressure distribution on the suction side of the airfoil at the flap root location. This discontinuity in the pressure for the 8015 configuration prevents the propagation of high-pressure regions upstream, reducing the adverse pressure gradient, and maintaining the suction peak near the leading edge of the airfoil. The suction side pressure discontinuity can be considered as a dam that prevents the propagation of higher pressures upstream, which
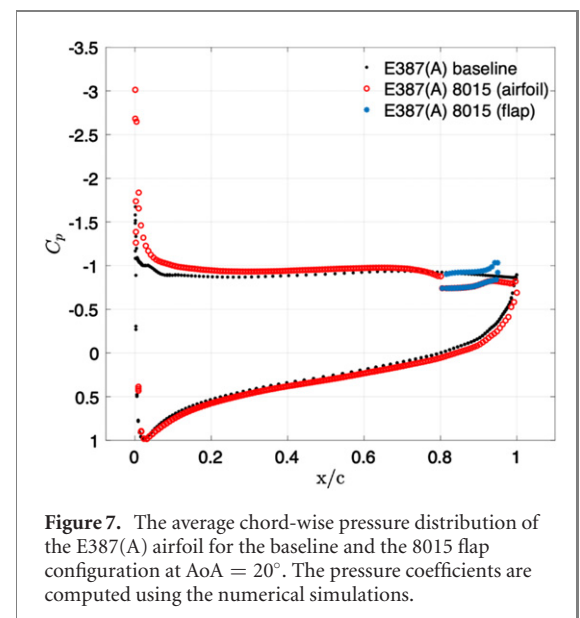

Figure 7. The average chord-wise pressure distribution of the E387(A) airfoil for the baseline and the 8015 flap configuration at AoA = 20°. The pressure coefficients are computed using the numerical simulations.

increases the overall lift produced by the airfoil. A similar pressure discontinuity, referred to as the pressure dam effect, was reported in the literature for soft stall airfoils with covert-inspired flaps [14, 16].

Effect of flap location: for the E387(A), the flap location has a significant effect on lift and drag. Mounting the flap at $0.7c$ (figure 8) instead of $0.8c$ (figure 6) reduces lift for all flap deflection angles and at both pre-stall and post-stall AoA. Moreover, moving the flap upstream (i.e. at $0.7c$) has negated the drag benefits observed at the more downstream location (i.e. at $0.8c$). This observation could be attributed to the relationship between the boundary layer thickness and the flap length. Typically, the boundary layer thickness is smaller at $0.7c$ when compared to $0.8c$. A flap of a fixed length and is deployed at the same deflection angle would protrude more into the boundary layer and the free stream at $0.7c$. Thus, moving the flap upstream may cause the flap to protrude into the freestream causing it to act more as a
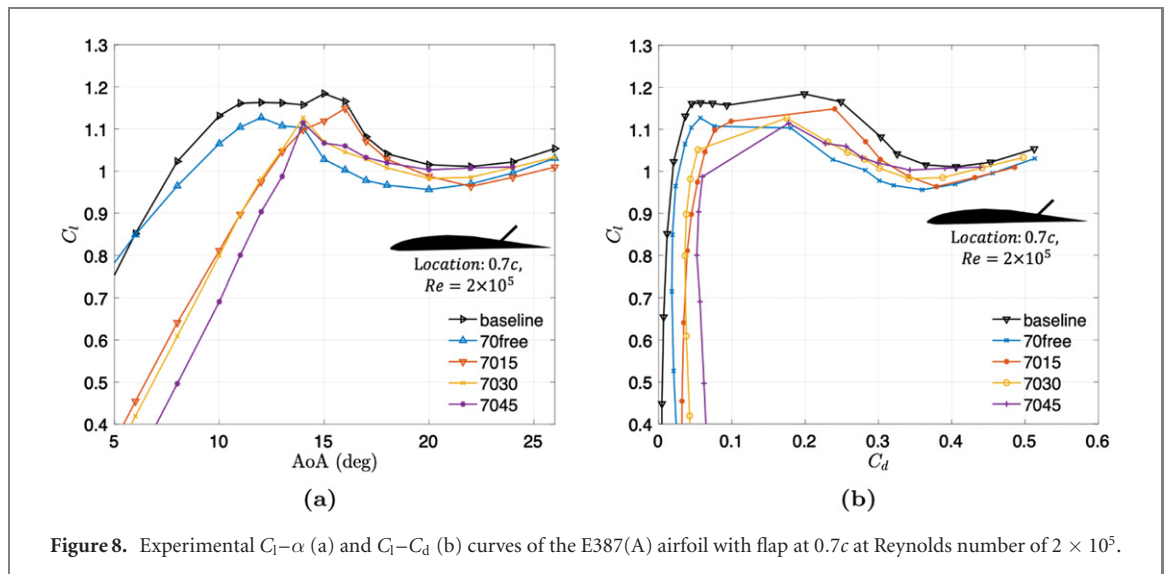
Figure 8. Experimental C_l–α (a) and C_l–C_d (b) curves of the E387(A) airfoil with flap at 0.7c at Reynolds number of 2×10^5.
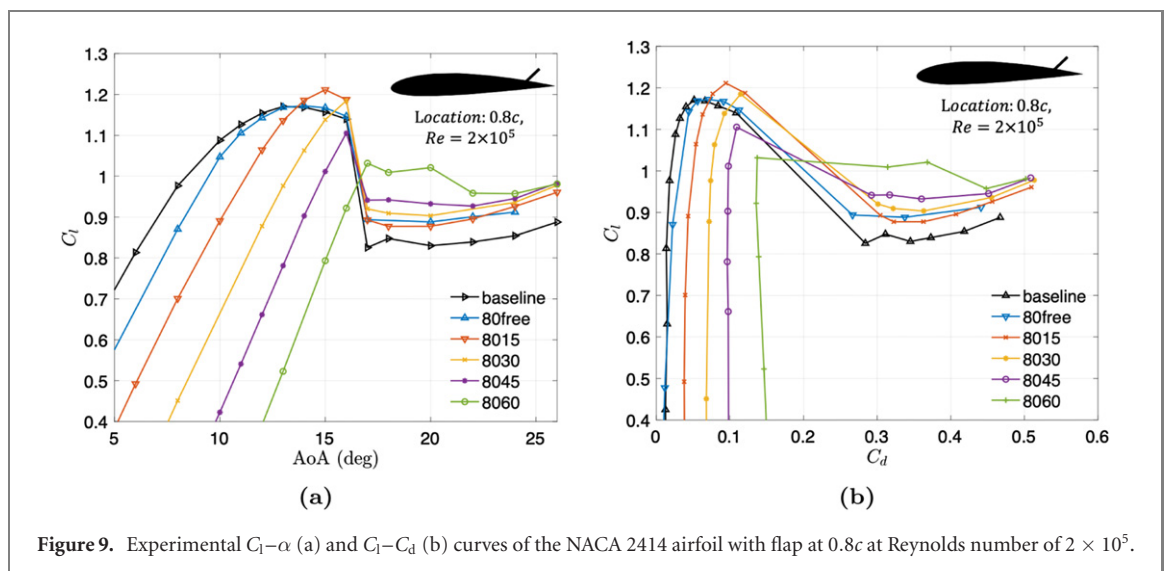

Figure 9. Experimental C_l–α (a) and C_l–C_d (b) curves of the NACA 2414 airfoil with flap at 0.8c at Reynolds number of 2×10^5.
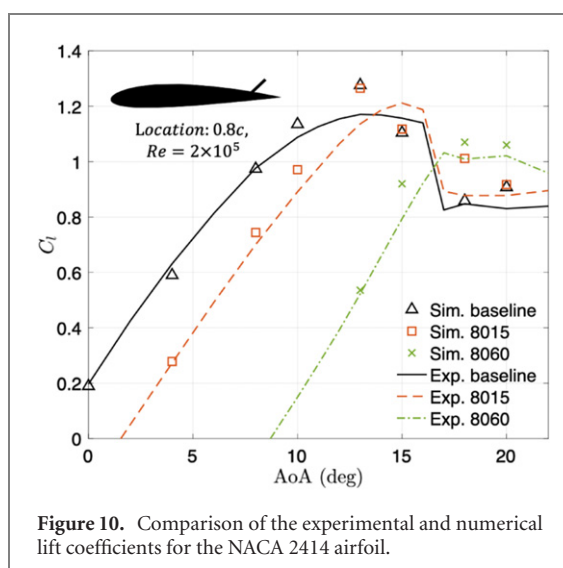

Figure 10. Comparison of the experimental and numerical lift coefficients for the NACA 2414 airfoil.

spoiler and less as a pressure modulation mechanism (i.e. figure 7). This explanation agrees with the results published in Meyer *et al* [15], where they indicated that a static flap yields maximum lift improvements when the flap just slightly touches the shear layer.

3.2. Sharp stall airfoil results

The NACA 2414 airfoil exhibits an abrupt stall when compared to the E387(A) airfoil. Figure 9 shows the C_l–α and the C_l–C_d curves for the NACA 2414 airfoil with a flap located at 0.8c at Re $= 2 \times 10^5$. Very few works in the literature have examined the effects of a covert-inspired flap on a sharp stall airfoil, thus this section presents an in depth discussion of the effect of the flap on the NACA2414.

Flap effect at pre-stall conditions: at the pre-stall angles of attack (AoA $< 16°$), the flap has the same
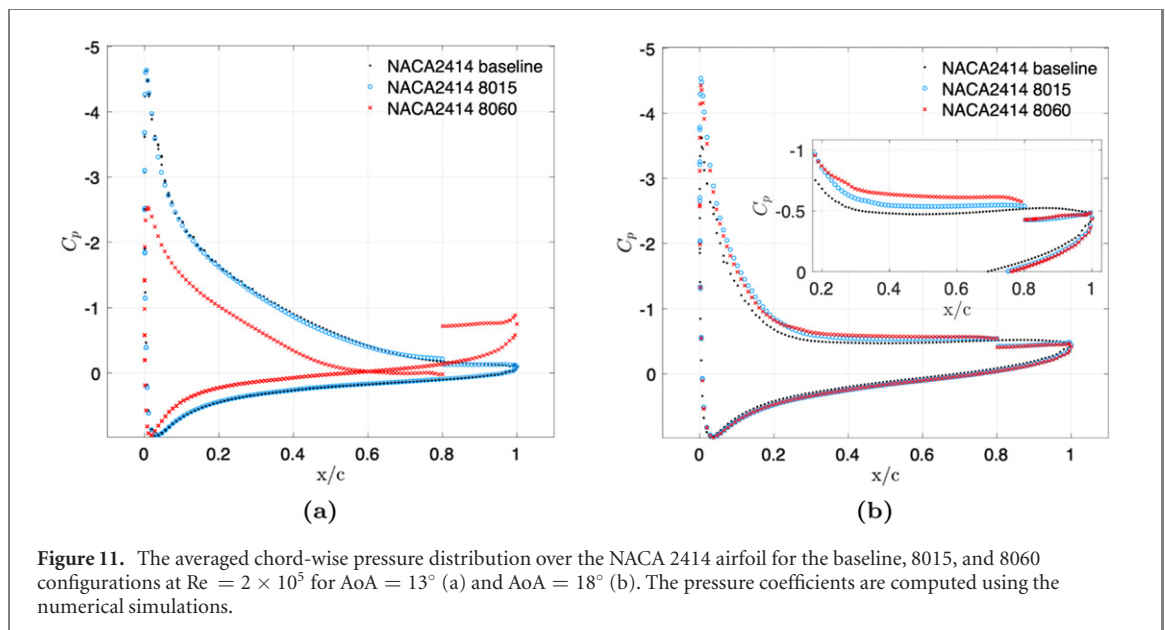
Figure 11. The averaged chord-wise pressure distribution over the NACA 2414 airfoil for the baseline, 8015, and 8060 configurations at Re $= 2 \times 10^5$ for AoA $= 13°$ (a) and AoA $= 18°$ (b). The pressure coefficients are computed using the numerical simulations.
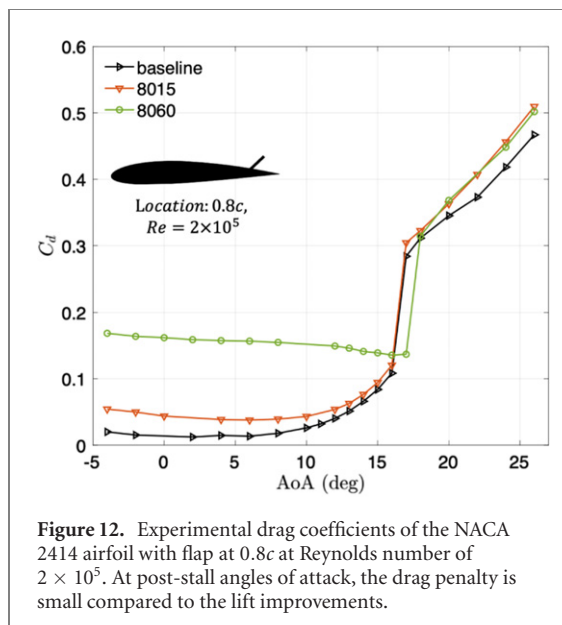

Figure 12. Experimental drag coefficients of the NACA 2414 airfoil with flap at $0.8c$ at Reynolds number of 2×10^5. At post-stall angles of attack, the drag penalty is small compared to the lift improvements.

overall effect as the E837(A) airfoil, including the pre-stall lift loss, drag increase, and slight C_{lmax} improvement. The static flap deflection angle has the same effect at pre-stall AoA for both the soft and sharp stall airfoils; the higher the deflection angle of the flap, the larger the lift penalty compared to the baseline airfoil. Moreover, similar to the soft stall airfoil, the freely-moving flap has reduced lift penalties compared to the static flap configurations due to its negligible deployment during pre-stall AoA.

The pre-stall loss of lift and reduction in aerodynamic efficiency can be explained by examining the numerical simulation results for the NACA 2414 airfoil. The numerical simulation lift results match experimental results with a relative error of less than 5% and 15% for the pre-stall and post-stall angles of attack, respectively (figure 10).

The numerical pressure distribution around the airfoil, C_p, explains the mechanisms that cause lift reduction at the pre-stall angles of attack (figure 11(a)). At AoA $= 13°$, when the flap is over-deflected (i.e. $\beta = 60°$), the pressure on the airfoil suction surface upstream the flap is significantly increased, while the pressure on the lower side of the airfoil is decreased, which results in the loss of lift shown in both the computational and the experimental results (figure 10). At the same AoA, deploying the flap at 15° does not change the baseline C_p distribution significantly. The only noticeable observation in C_p distribution is that there is a slight pressure step on the airfoil suction surface at the location of the flap root. Comparing the pressure distribution of the 8015 and 8060 flap configurations to the baseline explains why the loss of lift at this pre-stall AoA is lower for the 8015 flap configuration.

From the drag polar (figure 9(b)), the flap reduces aerodynamic efficiency at pre-stall angles of attack. The reduction in aerodynamic efficiency is due to the loss of lift (figures 9(a) and 11(a)) and the increase in drag (figure 12). The increase in drag can also be inferred by examining the wake behind the airfoil. Figure 13 shows the time-averaged velocity magnitudes around the NACA 2414 airfoil. A thicker red line is placed at the location of the flap. In the velocity contour plots, the wake size of each configuration is clearly shown by plotting the low-velocity region in the dark blue color. At the pre-stall AoA (i.e. AoA $= 13°$), the flow around the baseline airfoil is mildly separated from the trailing edge. The 8015 flap is not over-deflected and the wake size is similar to the baseline. In contrast, the 8060 flap protrudes into the free stream flow and significantly increases the wake size. An increase in the wake size supports the drag penalties observed in figure 12. At AoA $= 13°$, the drag produced by the 8015 configuration is slightly higher than
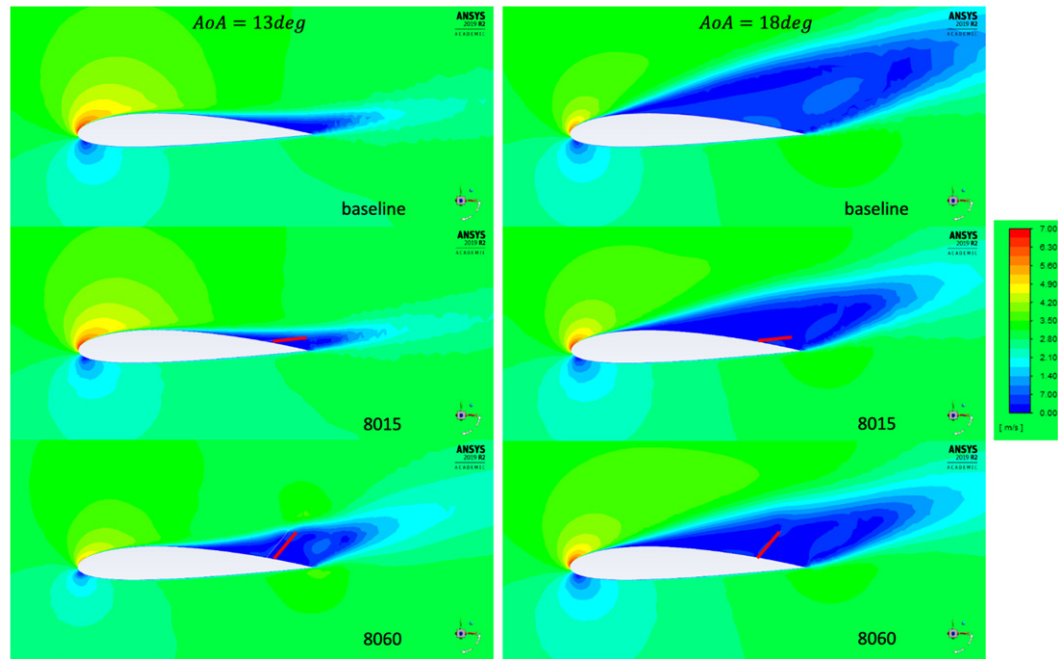
Figure 13. Numerical contour plots of the time-averaged velocity magnitude around the NACA 2414 baseline, 8015, and 8060 configurations at at Reynolds number of 2×10^5 for AoA $= 13°$ (left) and AoA $= 18°$ (right).
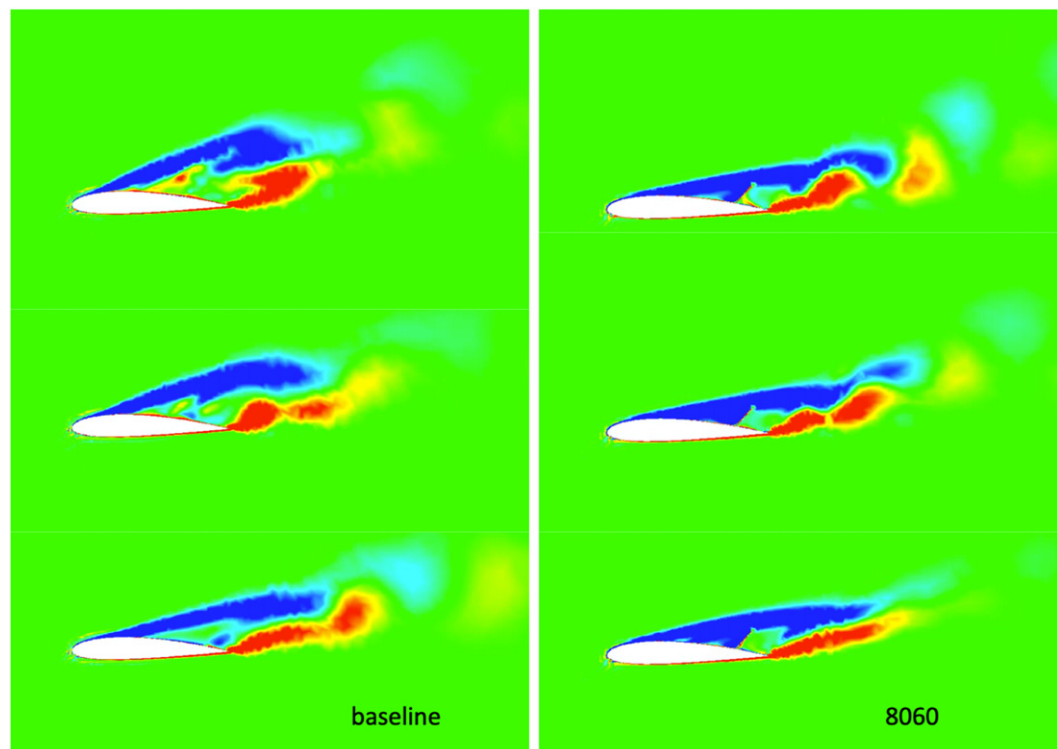
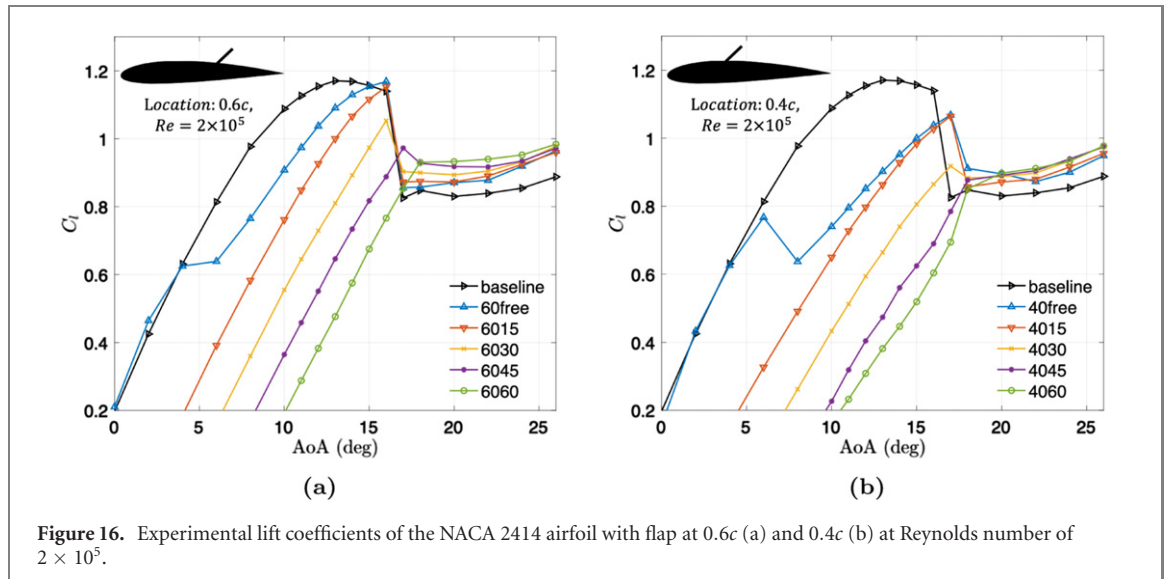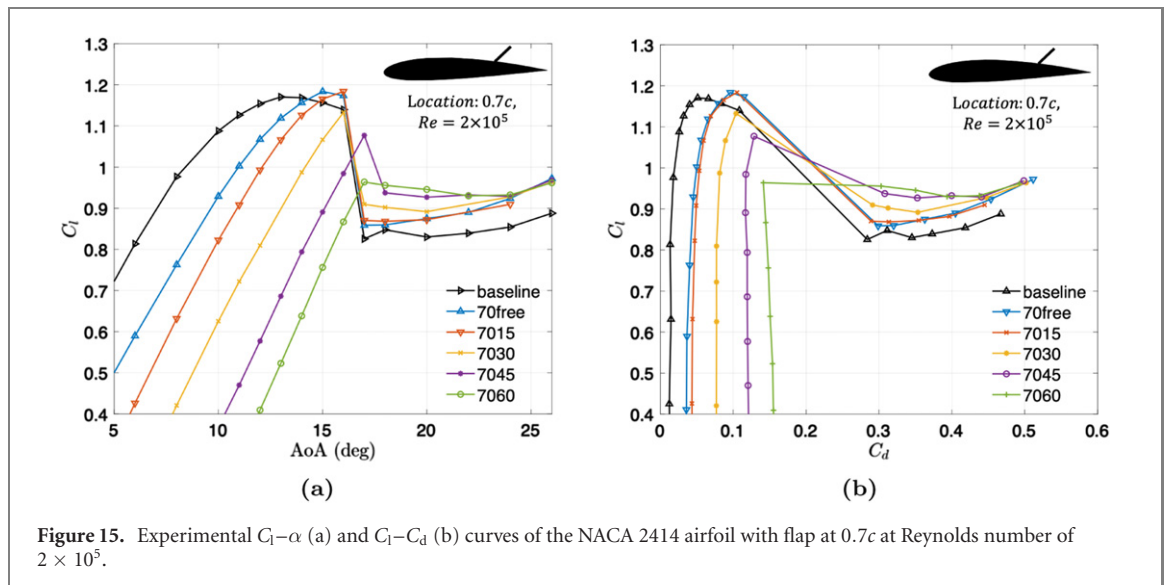
Figure 14. Numerical contour plots of the instantaneous span-wise vorticity, W_z, for the baseline NACA 2414 airfoil (left) and the 8060 configuration (right) at AoA $= 18°$ and Re $= 2 \times 10^5$. Blue, negative vorticity; red, positive ($\pm 7 U_\infty / c$). All snap shots represent maximum lift time instances.

the baseline ($\approx 22\%$), while there is a significant drag penalty for the 8060 configuration ($\approx 285\%$).

Flap effect at post-stall conditions: at the post-stall angles of attack (AoA $> 16°$), the flap on the NACA 2414 airfoil does not delay stall as it did on the soft stall airfoil. No significant change in the stall AoA is observed in figure 9(a). Both the baseline airfoil and airfoil with the flap airfoil stall at AoA $= 16°$, the only exception is for the 8060 flap configuration, where stall occurs at AoA $= 17°$ instead of $16°$. However, the

Figure 15. Experimental $C_l-\alpha$ (a) and C_l-C_d (b) curves of the NACA 2414 airfoil with flap at 0.7c at Reynolds number of 2×10^5.

Figure 16. Experimental lift coefficients of the NACA 2414 airfoil with flap at 0.6c (a) and 0.4c (b) at Reynolds number of 2×10^5.

NACA 2414 airfoil with the flap mounted on the suction side still improves the post-stall lift compared to the baseline, which significantly reduces the lift loss at these high angles of attack. Lift improvements up to 23% lift is observed for the 8060 flap at AoA = 20°. Figure 9(b) shows that the flap also enhances the aerodynamic efficiency. For the same drag, the airfoil with the flap produces more lift when compared to the baseline airfoil. Moreover, unlike the soft stall airfoil, the post-stall lift improvement of the NACA 2414 airfoil is sensitive to the flap deflection angle, where higher flap deflection angles resulted in more lift improvement. The sensitivity of the post-stall lift improvements to the flap deflection angle suggests that the lift improvements can be tuned.

Examining the numerical pressure distribution, vorticity field, and velocity contours offer an explanation for these observations. At AoA = 18°, which is a post-stall AoA, the pressure step is more visible than

for AoA = 13° (figure 11(b)). Compared to the baseline, the pressure upstream of the flap is decreased, which creates more suction on the upper surface, while the pressure downstream of the flap is increased, which results in a lift penalty in that region. However, the favorable effect of the flap upstream is larger than its adverse effect. Thus, the total change in the pressure distribution leads to enhanced lift generation. The 8060 flap configuration creates a larger pressure step between the pressure upstream and downstream of the flap, which results in a larger lift improvement compared to the 8015 configuration. The variation of the pressure step size supports the sensitivity of the lift improvements to the flap deflection as observed in the $C_l-\alpha$ plots (figure 9(a)).

The vorticity field around the airfoil also provides insights into the post-stall lift enhancement mechanisms. Figure 14 shows the contour plots of the instantaneous span-wise, z component of vorticity W_z for the baseline NACA 2414 airfoil and the NACA

2414 with 8060 flap at AoA = 18° at three different instances. Each of these three instances corresponds to a peak in the lift time history. In all instances and for both configurations, negative vorticity is observed near the leading edge. However, for the 8060 flap configuration, the negative vorticity is closer to the surface of the airfoil when compared to the baseline. Being close to the airfoil surface facilitates the persistent collection of negative vorticity from the shear layer on the suction side, which corresponds to an increase in the lift compared to the baseline vorticity, which is further from the surface. The vorticity field confirms the lift measurements and explains the improvements in the pressure distribution upstream of the flap.

At post-stall AoA, the flap on the NACA 2414 airfoil enhances the aerodynamic efficiency (figure 9(b)). The aerodynamic efficiency improvements are due to an increase in lift (figure 9(a)) for a negligible drag penalty (less than 5%). Moreover, while the lift enhancement is sensitive to the flap deflection angles, the post-stall drag is insensitive to the flap deflection angle (figure 12). The insensitivity of the drag penalty to the flap deflection angle can be confirmed by observing the wake behind the airfoil. At AoA = 18°, the velocity contours in figure 13 shows that the flow over the baseline airfoil is separated massively. Mounting the flap on the suction side of the airfoil slightly mitigated the flow separation over the airfoil compared to the baseline. However, changing the flap deflections angle from 15° to 60° has a negligible effect on the wake profile behind the airfoil. These observations support the drag data (figure 12), which show comparable drag for all three configurations namely, the baseline, 8015, and 8060 configurations.

Effect of flap location: finally, the effect of the flap location on lift and drag depends on the baseline airfoil choice. Unlike the soft stall airfoil, the flap mounted at 0.7c on the NACA 2414 airfoil is still effective in improving post-stall lift (figure 16). These post-stall lift improvements are still observed even as the flap is moved more upstream to to 0.6c and 0.4c, as shown in figure 16. However, comparing figures 9(a) to figure 15(a) shows that while the over all effects of the flap on lift remains the same across flap locations, the deflection angle that leads to the most pronounced lift improvements is different. This difference supports the observation made by Meyer *et al* [15], which states that the optimal flap deflection is the one that slightly touches the separated shear layer. Therefore, as the flap location moves upstream, for the same length of the flap, the flap deflection angle that slightly touches the shear layer decreases. Thus, for the flap location of 0.7c, the optimal flap deflection is 45° and for the flap location of 0.4c, the optimal flap deflection is 30°, while for the flap location of 0.8c, the optimal flap deflection is 60°.

4. Conclusion

This study explores how the choice of the base airfoil changes the effect of a covert-inspired flap on lift and drag at the Reynolds numbers of 2×10^5. A single covert-inspired flap was mounted on two baseline airfoils, one with a gradual stall behavior (i.e. the E387(A)), and another with an abrupt stall (i.e. the NACA 2414). Both wind tunnel experiments and numerical simulations were carried out to determine the effects of the covert-inspired flap on lift and drag at pre-stall and post-stall angles of attack, and the effects of varying the chord-wise location of the flap. Most prior studies focused on analyzing the flap effects on airfoils with softer stall behavior. Thus, this study pays more attention to the flap effects on the NACA 2414 airfoil, which exhibits an abrupt stall behavior.

The results show that while pre-stall lift penalties and drag increase, as well as post-stall lift and aerodynamic efficiency enhancements are common to both airfoils, the specific characteristics of the post-stall lift enhancements are different. Examining the integrated forces, pressure distribution, instantaneous vorticity fields, and velocity contours, the main study conclusions are as follows:

- For a covert-inspired flap on a soft stall airfoil:

1. The post-stall lift improvements is attributed to a pressure step on the suction side of the airfoil. This step is refereed to as a pressure dam, and was first proposed by Bramesfeld and Maughmer [14]. These lift improvements are also accompanied by a noticeable delay in stall.

2. At post-stall angles of attack, the lift improvements are insensitive to the flap deflection angle. Changing the flap deflection does not modulate the post-stall lift improvements.

3. The post stall lift and aerodynamic efficiency improvements are highly sensitive to the flap location. A 10% change in the chord-wise location renders the flap ineffective in improving lift.

- For a covert-inspired flap on a sharp stall airfoil:

1. The lift improvements are due to the pressure dam effect and the proximity of the negative vorticity to the suction side of the airfoil upstream of the flap. Unlike the soft stall airfoil, there is no noticeable delay in stall, only reduction in the lift drop after stall.

2. The post-stall lift improvements are sensitive to the flap deflection angle. Changing the flap angle modulates the strength of the pressure dam. In contrast, the post-stall drag is insensitive to the flap deflection angle.

The integrated drag and velocity wake profile behind the airfoil remain the same for all flap deflection angles.

3. The flap remains effective in improving the post-stall lift for various flap locations ranging from $0.4c$ to $0.8c$

The choice of the airfoil changes the characteristics of the post-stall lift enhancement associated with a covert-inspired flap. For the sharp stall airfoil, the flap effectiveness at multiple locations suggests the potential for a multiple flap design that could help augment lift over a very wide range of AoA. Moreover, the difference in the lift improvement sensitivities indicates that for the sharp stall airfoil the flap can be used as a tunable flow control device, while for the soft stall airfoil it can solely be used as a stall mitigation device that is either on or off. Finally, the lift improvements in the post-stall regime did not induce significant drag penalties. Such property can be used to control rolling moment without affecting the yawing moment, reducing common undesirable effects such as adverse yaw. The findings of this study can guide the design and adaptation of a covert-inspired flap for lift enhancement and mitigating stall in small scale UAVs.

Acknowledgments

Data availability statement

The data that support the findings of this study are available upon reasonable request from the authors.

ORCID iDs

Chengfang Duan ⓘ https://orcid.org/0000-0002-4428-6640
Aimy Wissa ⓘ https://orcid.org/0000-0002-8468-511X

References

[1] Evers J H 2007 Biological inspiration for agile autonomous air vehicles *Technical Report* Air Force Research Lab, Eglin AFB, Munitions Directorate
[2] Lissaman P B S 1983 Low-Reynolds-number airfoils *Annu. Rev. Fluid Mech.* **15** 223–39
[3] Taylor G K, Carruthers A C, Hubel T Y and Walker S M 2012 Wing morphing in insects, birds and bats: mechanism and function *Morphing Aerospace Vehicles and Structures* pp 13–40
[4] Videler J J 2006 *Avian Flight* (Oxford: Oxford University Press)
[5] Carruthers A C, Thomas A L R and Taylor G K 2007 Automatic aeroelastic devices in the wings of a Steppe eagle *Aquila nipalensis J. Exp. Biol.* **210** 4136–49
[6] Brown Richard E and Fedde M Roger 1993 Airflow sensors in the Avian wing *J. Exp. Biol.* **179** 13–30
[7] Alexas_Fotos/Pixabay 2017 https://pixabay.com/photos/snow-owl-flying-bubo-scandiacus-2425159/
[8] Kevinsphotos/Pixabay 2016 https://pixabay.com/photos/steppe-eagle-eagle-steppe-nature-1576898/
[9] Wang L, Alam M M and Zhou Y 2019 Experimental study of a passive control of airfoil lift using bioinspired feather flap *Bioinspir. Biomim.* **14** 066005
[10] Brücker C and Weidner C 2014 Influence of self-adaptive hairy flaps on the stall delay of an airfoil in ramp-up motion *J. Fluid Struct.* **47** 31–40
[11] Gardner A D, Opitz S, Wolf C C and Merz C B 2017 Reduction of dynamic stall using a back-flow flap *CEAS Aeronaut. J.* **8** 271–86
[12] Bechert D, Bruse M, Hage W, Meyer R, Bechert D, Bruse M, Hage W and Meyer R 1997 Biological surfaces and their technological application-laboratory and flight experiments on drag reduction and separation control *28th Fluid Dynamics Conf.* p 1960
[13] Bechert D W, Bruse M, Hage W and Meyer R 2000 Fluid mechanics of biological surfaces and their technological application *Naturwissenschaften* **87** 157–71
[14] Bramesfeld G and Maughmer M D 2002 Experimental investigation of self-actuating, upper-surface, high-lift-enhancing effectors *J. Aircraft* **39** 120–4
[15] Meyer R, Hage W, Bechert D W, Schatz M, Knacke T and Thiele F 2007 Separation control by self-activated movable flaps *AIAA J.* **45** 191–9
[16] Johnston J and Gopalarathnam A 2012 Investigation of a bio-inspired lift-enhancing effector on a 2d airfoil *Bioinspir. Biomim.* **7** 036003
[17] Fang Z, Gong C, Revell A, Chen G, Harwood A and O'Connor J 2019 Passive separation control of a NACA0012 airfoil via a flexible flap *Phys. Fluids* **31** 101904
[18] Schlüter J U 2010 Lift enhancement at low Reynolds numbers using self-activated movable flaps *J. Aircraft* **47** 348–51
[19] Ito M R, Duan C, Chamorro L P and Wissa A A 2018 A leading-edge alula-inspired device (lead) for stall mitigation and lift enhancement for low Reynolds number finite wings *ASME 2018 Conf. on Smart Materials, Adaptive Structures and Intelligent Systems* (American Society of Mechanical Engineers Digital Collection)
[20] Giguère P and Selig M S 1997 Freestream velocity corrections for two-dimensional testing with splitter plates *AIAA J.* **35** 1195–200
[21] Ito M R, Duan C and Wissa A A 2019 The function of the alula on engineered wings: a detailed experimental investigation of a bioinspired leading-edge device *Bioinspir. Biomim.* **14** 056015
[22] Barlow J B, Rae W H Jr and Pope A 2015 *Low Speed Wind Tunnel Testing* 7 (INCAS - National Institute for Aerospace Research "Elie Carafoli")
[23] Selig M S, Guglielmo J J, Broeren A P and Giguere P 1995 *Summary of Low Speed Airfoil Data* vol 1–3 (Virginia Beach, Virginia: SoarTech Aero Publications)
[24] Shur M, Spalart P R, Strelets M and Travin A 1999 Detached-eddy simulation of an airfoil at high angle of attack *Engineering Turbulence Modelling and Experiments* vol 4 (Amsterdam: Elsevier) pp 669–78